

Author Manuscript

Title: Enantiomeric Discrimination by Surface-Enhanced Raman Scattering-Chiral Anisotropy of Chiral Nanostructured Gold Films

Authors: Zexi Liu; Jing Ai; Prashant Kumar; Enming You; Xiong Zhou; Xi Liu; Zhongqun Tian; Petr Bouř; Yingying Duan; Songyuan Ding; Lu Han; Nicholas Kotov; Shunai Che, Ph.D.

This is the author manuscript accepted for publication and has undergone full peer review but has not been through the copyediting, typesetting, pagination and proofreading process, which may lead to differences between this version and the Version of Record.

To be cited as: 10.1002/ange.202006486

Link to VoR: <https://doi.org/10.1002/ange.202006486>

Enantiomeric Discrimination by Surface-Enhanced Raman Scattering-Chiral Anisotropy of Chiral Nanostructured Gold Films

Zexi Liu,[†] Jing Ai,[†] Prashant Kumar,[†] Enming You,[†] Xiong Zhou,[†] Xi Liu,[†] Zhongqun Tian, Petr Bouř, Yingying Duan, * Nicholas A. Kotov,* Songyuan Ding,* Lu Han* and Shunai Che*

Abstract: Here, we report surface-enhanced Raman scattering-chiral anisotropy (SERS-ChA) effect that combines chiral discrimination and surface Raman scattering enhancement on chiral nanostructured Au films (CNAFs) equipped in the normal Raman scattering Spectrometer. The CNAFs provided remarkably higher enhancement factors of Raman scattering (EFs) for particular enantiomers, and the SERS intensity was proportional to the enantiomeric excesses (*ee*) values. Except for molecules with mesomeric species, all of tested enantiomers exhibited high SERS-ChA asymmetry factors (*g*), ranging between 1.34 and 1.99 regardless of polarities, sizes, chromophores, concentrations and *ee*. The effect might be attributed to selective resonance coupling between the induced electric and magnetic dipoles associated with enantiomers and chiral plasmonic modes of CNAFs.

Enantiomeric discrimination is of critical importance in many areas of analytical sciences, chemical biology, pharmacy and pesticide science.^[1] Multiple theoretical concepts and chiroptical spectroscopic techniques, such as optical rotation and circular dichroism, have been developed to detect and quantify enantiomers. Typically, circularly polarized light is used to identify the absolute configuration and composition of enantiomers (Table S1).^[2] However, these methods are impossible to use for racemates or compounds with weak optical response.^[3]

Surface-enhanced Raman spectroscopy is a powerful technique that provides ultra-sensitive structural information

interaction of molecules with the strong electromagnetic field^[5] localized around metallic nanostructures which also contributes to strong radiation enhancement. The polarized analogue of SERS, surface-enhanced Raman optical activity (SEROA) was also proposed as a technique to identify enantiomers, using difference in SERS of left- and right-handed circularly polarized light (Figure S1). However, similar to other methods employing OA (Table S1), SEROA^[6] provides relatively weak anisotropic signal (ROA/Raman ratio), and is useless for racemates.

We investigate a different approach, where the chiral anisotropy is created by a highly polarizable chiral platform that can discriminate enantiomers *via* SERS using linearly polarized or unpolarized light (Figure 1a, Figure S1). The described SERS-ChA method is, thus, based on a selective SERS EF of enantiomers on a chiroplasmonic surface, which provides high enantiomeric sensitivity (Figure 1b). Observable parameters in SERS-ChA are defined as the difference in SERS intensities of enantiomeric molecules on the same chiral platform, $SERS-ChA = I_S - I_R$, where I_S and I_R are SERS intensities of S- and R-enantiomers, respectively (Figure 1b). The *g*-factor is defined in a usual way, as $g_{SERS-ChA} = 2(I_S - I_R)/(I_S + I_R)$. The maximum $\lim|g|_{max} = 2$ indicates a complete discrimination of enantiomers. Detecting and quantifying an unknown sample (Figure 1c) require a calibration curve, obtained for enantiomers as Raman intensity dependent of the *ee* values from -100% to +100% at known concentrations. The *g*-factor can be obtained from the slope (*k*) and intercept (*b*) of curve: $g_{SERS-ChA} = 2k/b$. The tested compound is then diluted to the concentration employed in the SERS-ChA standard curve to determine the Raman intensity and the corresponding *ee* value on the chiral plasmonic platform. The enantiomeric resolution system with SERS-ChA overcome the disadvantages of SEROA^[7] (Figure S1). It can also be used for any enantiomers regardless of their electric dipole, size, and functionality, which often problematic for chiral chromatography.

[*] Z. Liu,^[†] J. Ai,^[†] Dr. Y. Duan, Prof. L. Han, Prof. S. Che
School of Chemical Science and Engineering, Tongji University,
1239 Siping Road, Shanghai, 200092 (P.R. China)
E-mail: chesa@tongji.edu.cn
yyduan@tongji.edu.cn
luhan@tongji.edu.cn
Homepage: <http://che.tongji.edu.cn>
Prof. S. Che
School of Chemistry and Chemical Engineering, State Key
Laboratory of Metal Matrix Composites, Shanghai Jiao Tong
University, 800 Dongchuan Road, Shanghai, 200240 (P.R. China)
Dr. P. Kumar,^[†] Prof. Nicholas A. Kotov
Department of Chemical Engineering and Biointerfaces Institute,
University of Michigan, Ann Arbor, Michigan 48019 (United States)
E-mail: kotov@umich.edu
Prof. Z. Tian, Prof. S. Ding
College of Chemistry and Chemical Engineering, Xiamen University,
Xiamen, 361005 (P.R. China)
E-mail: syding@xmu.edu.cn
Dr. X. Zhou, Dr. X. Liu
SynCat@Beijing, Synfuels China Technology Co., Ltd, Beijing
101407 (P.R. China)
Prof. P. Bouř
Institute of Organic Chemistry and Biochemistry, Czech Academy of
Sciences, Flemingovo náměstí 2, 16610, Prague (Czech).

[†] These authors contributed equally to this work.

Supporting information for this article is given via a link at the end of the document.

through the vibrational “fingerprint” of trace analytes,^[4] due to the

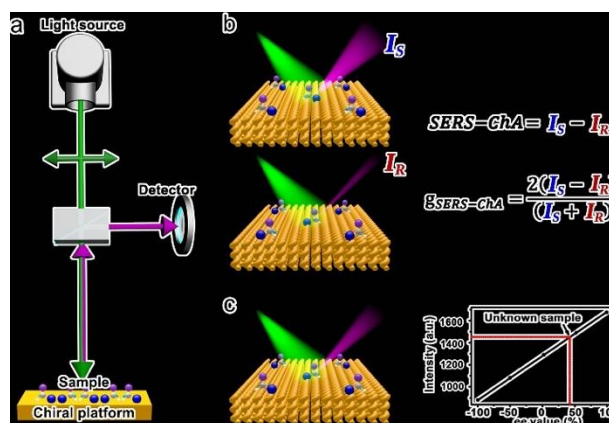


Figure 1. Schematic illustration of the SERS-ChA method for enantiomer discrimination. a) Conventional Raman scattering equipment with a chiral platform. b) SERS-ChA and *g*-factor are obtained for enantiomeric molecules. c) Absolute configurations and *ee* values of unknown samples can be obtained from the calibration curves.

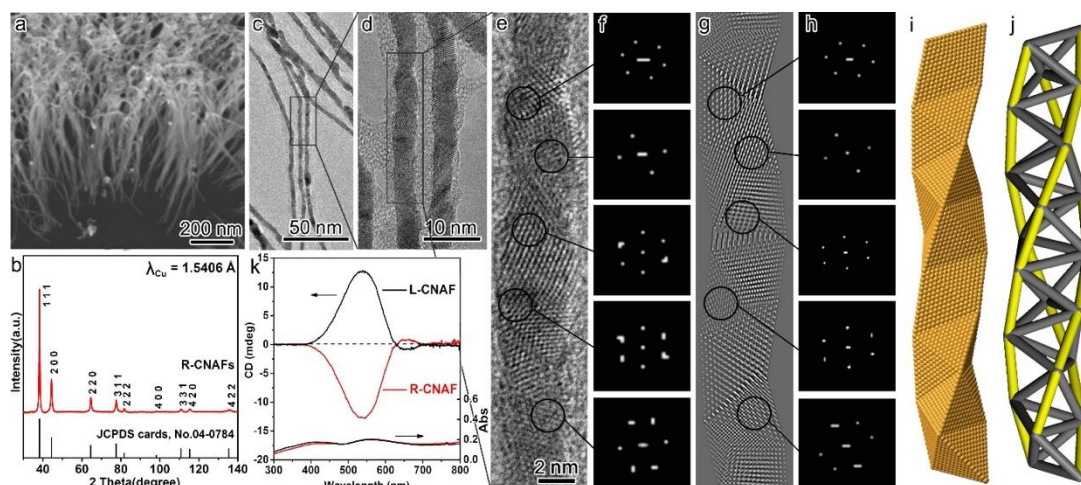


Figure 2. Morphologies and structures of R-CNAFs. a) Low-magnification SEM image of Au nanofibres vertically grown on a Si wafer. b) The XRD pattern demonstrates that the Au crystals display a *fcc* structure and preferably grow along the $\langle 111 \rangle$ direction. c) Low-magnification TEM images of Au nanofibres that were mechanically removed from the wafer, showing twisting in almost all fibres. d) High-magnification TEM image of Au nanofibres showing a polycrystalline structure. e, f) HRTEM image and corresponding FDs of an Au fibre with an ideal BCB structure. g, h) Simulated TEM image and FDs showing good agreement with experimental observations. i) Schematic drawing of a right-handed chiral Au fibre, showing the BCB helix configuration from multiply twinned tetrahedral Au nanocrystals with a face-sharing relationship. j) A triple helix is revealed by connecting the outside edges of the stacked tetrahedra (yellow line). The synthetic chemical molar composition of R-CNAF was S-NAC: 4-MBA: HAuCl_4 : AA = 15:8:25:40. Tip: The shadowed area around the fibre in the TEM image is the shrunk carbon film under electron beam irradiation (see Figure S8 for the shrinking process).

Here, we fabricated a chiral platform for SERS-ChA consisting of arrays of CNAFs on various silicon-containing wafers, such as single-crystal silicon [Si (100)], quartz, and glass, *via* an amino acid-induced symmetry-breaking route (Figure S2). The wafer was lithographically ablated to generate cylindrical holes (Figure S2a, b) that served as sample cells for the quantitative detection of enantiomeric compounds in solution. The helical Au fibres were prepared in four steps by direct epitaxial growth on the substrate surface. (i) The substrate was first activated using a $\text{H}_2\text{SO}_4/\text{H}_2\text{O}_2$ mixture with an abundance of silanol groups on the surface (Figure S2c). (ii) Amino groups were modified to the surface *via* condensation of the silanols and the siloxane of 3-aminopropyltriethoxysilane to terminate the substrate surface (Figure S2d). (iii) A gel mixture composed of N-Acetyl-L/D-cysteine (S/R-NAC), 4-mercaptobenzoic acid (4-MBA), HAuCl_4 , (2S, 3R)-ascorbic acid (AA), and H_2O was subsequently introduced onto the substrate. 4-MBA acts as a coating agent, and AA reduces Au^{3+} ions to Au^0/Au^+ during the helical growth of chiral Au nanofibre arrays on the wafer to form as-prepared CNAFs (Figure S2e). The S/R-NAC would act as a symmetry-breaking agent in the helical fibre growth because the asymmetric arrangement of Au-S, Au-NH₂, and Au-COO bonds around the chiral carbon centre regulates the Au crystal morphology. Moreover, CNAFs could not be obtained using the same fabrication route in the absence of NAC. The fibre growth followed a seed (Figure S3) mediated growth process through reducing Au at the interface between substrate and seeds.^[8] (iv) Organic components were removed *via* electrochemical oxidation to produce chiral platforms of pure inorganic CNAFs (Figure S2f and S4), which was confirmed by Raman spectroscopy (Figure S5). S- and R-NAC enantiomers led to right handed CNAFs (R-CNAFs) and left-handed CNAFs (L-CNAFs), respectively, which were confirmed from their structural orientation and their different responses to circularly polarized light (*vide post*).

Figure 2a shows scanning electron microscopy (SEM) images of R-CNAFs grown on a Si (100) wafer with lithographically ablated cylinder holes. The films consist of densely packed Au nanofibres with a uniform length of ~ 500 nm

grown vertically on the surface of the silicon substrate. The crystalline structure of R-CNAF was analysed by wide-angle X-ray diffractometry (XRD) (Figure 2b). The reflections indicate that R-CNAF adopts the typical face-centred cubic (*fcc*) structure of Au in the space group $Fm\bar{3}m$ (JCPDS 04-0784) without any additional peaks. The relative intensity of $\{111\}$ is much higher in R-CNAFs than in the bulk sample suggesting the preferred orientation along the $\langle 111 \rangle$ direction in the Au fibres and dominance of $\{111\}$ planes formed by the stacking of the tetrahedral Au nanoparticles (*vide post*).

A low-magnification transmission electron microscopy (TEM) micrograph (Figure 2c) shows that almost all Au nanofibres present a helically twisting-like morphology and uniform diameters of ~ 5.5 nm. These helical nanofibres display a polycrystalline structure at high magnification (rectangular area, Figure 2c and 2d). The high-resolution TEM (HRTEM) image of a single Au nanofibre (Figure 2e) indicates that the tetrahedral units of the Au nanocrystals stacked into a so-called Boerdijk-Coxeter-Bernal (BCB) *tetrahelix*^[9]. The surface energy of *fcc* crystals, such as Au, follows the order $\gamma\{111\} < \gamma\{100\} < \gamma\{110\}$. Therefore, the octahedral or tetrahedral shape is preferred to maximize the exposure of $\{111\}$ facets. In the current work the Au nanocrystals also have a tetrahedral shape, and the nanofibres consist of stacked tetrahedra that share their $\{111\}$ facets in a multiply twinned manner. A right-handed *in silico* BCB model was built to interpret the helical structure: each tetrahedral nanocrystal is connected by twin boundaries that bind adjacent $\{111\}$ facets (Figure 2i and j). The simulated HRTEM image^[10] and the corresponding Fourier diffractograms (FDs) from different structural domains of the nanofibre show good agreement with the observed HRTEM images and the FDs (Figure 2e-h), which confirms that the structural model is realistic (Figure 2i and 2j). A few Au fibres also adopt imperfect BCB structures (Figure S6). Perfect and imperfect *tetrahelices* of R-CNAFs appear as right-handed triangular spirals. The L-CNAFs gave similar profiles with the same sizes and quality (Figure S7). The handedness of antipodal CNAFs was also confirmed by their different responses to circular polarized light (*vide post*).

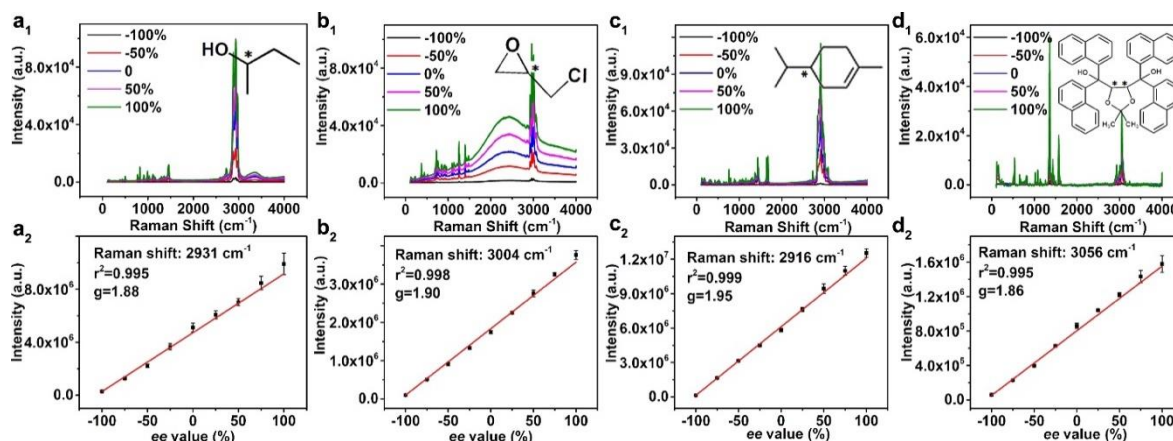


Figure 3. Examples of the SERS-ChA effect of R-CNAFs. Raman spectra (top) and dependencies (bottom) of the largest SERS peak areas on ee values, from -100% to +100% for four sets of enantiomers. a₁, a₂) 2-Butanol (MW:74.1). b₁, b₂) Epichlorohydrin (MW:92.5). c₁, c₂) Limonene (MW:136.2). d₁, d₂) 2,2-Dimethyl- $\alpha,\alpha,\alpha',\alpha'$ -tetra(1-naphthyl)-1,3-dioxolane-4,5-dimethanol (MW:666.8).

The universality of the SERS-ChA effect was investigated by placing 100 pairs of commercially available enantiomers with different electric dipole configurations, sizes, chromophores, concentrations, and ee values (Table S2) on R-CNAFs. Figure 3 shows the enantiomeric discrimination results of four typical enantiomeric compounds presenting at least one of the following properties: small or large molecular weight, low polarity, and chromophore-free structure, which are difficult to be applicable to chromatography or chiroptical spectroscopy. The four compounds were 2-butanol (Figure 3a), epichlorohydrin (Figure 3b), limonene (Figure 3c) and 2,2-dimethyl- $\alpha,\alpha,\alpha',\alpha'$ -tetra(1-naphthyl)-1,3-dioxolane-4,5-dimethanol (Figure 3d).

As a typical example, the Raman spectra of 2-butanol were compared for ee values varying from -100% to +100% (Figure 3a₁). All peak areas for characteristic Raman scattering of enantiomers show good linear correlations with the ee value (Figure 3a₂ and S9a₁). SERS intensities of S-enantiomers are nearly two orders of magnitude higher than those of their R analogues, indicating highly selective SERS enhancement of antipodal enantiomers on R-CNAFs. The normalized linear curves for each scattering peak show identical trend, a linear correlation between each SERS peak area and the ee value (Figure S9a₂). The *g*-factor of antipodal 2-butanol on R-CNAFs was 1.87 ± 0.02 obtained from the slopes of calibration curves using each detectable Raman peak area (Figure S9a₁), which reveals fundamentally different Raman scattering behaviour between two enantiomers and the same selectivity for all vibrational bands. The other three sets of model enantiomers exhibit a similar correlation between SERS signals and ee values, with high *g*-factors of 1.90, 1.95 and 1.85 (Figure 3b-3d and S9b-d). With the exception of the molecules displaying the same amounts of mesomeric species, 98 pairs of the 100 enantiomers can be discriminated with high *g*-factors ranging from 1.34-1.99 (Table S2), indicating the high discrimination capacity of CNAFs. The *g*-factors seem independent of any molecular features, including size, nature and number of functional groups, electric dipole configuration, and presence of chromophores. The SERS-ChA effect of CNAFs could be efficient in a wide range of ee.

The specimen loading amount per unit area was optimised to eliminate the influence of molecular amounts on the surface so that the SERS intensity expresses the intrinsic properties of CNAFs. This optimisation was performed by measuring the *g*-factor and SERS intensity for different enantiomer loading amounts ranging between 2.5×10^{-11} and 7.5×10^{-6} mol/mm²

(Figure S10) The measured *g*-factors remained almost constant at loading rates ranging from 2.5×10^{-9} to 7.5×10^{-8} mol/mm² while the SERS intensity remained high between 2.5×10^{-9} and 2.5×10^{-8} mol/mm² for the four types of enantiomers. This indicates that having an inadequate or an excess number of molecules outside the CNAFs decreases the accuracy of its discrimination, as expected. To ensure a high signal-to-noise ratio and clear SERS-ChA effect on CNAFs, SERS measurements were performed at a relatively high loading (2.5×10^{-8} mol/mm²) and with constant *g*-factors. The consistency and homogeneity of the film, which ensure the accuracy of SERS-ChA, were confirmed for nine different films fabricated according to the same preparation parameters and nine different cylinder cells, respectively (Figure S11, Table S3 and S4). The error of the *g*-factor for films and cylinder cells was 0.1% and 0.2%, respectively. Other test indicates that the SERS-ChA effect is stable with respect to pH (Figure S12), mixtures with achiral / chiral interferences (Figure S13-14) and mixture enantiomers (Figure S15), and reproducible (Table S3-S4) for real world sample.

The *g*-factors of both racemic CNAFs and achiral nanostructured Au films (NAFs) were zero (Figure S16a-b) and that of L-CNAFs was negative (Figure S16e). The enhancement in Raman intensities of R-CNAFs loaded with racemic molecules was 35 and 200 times greater than those of racemic CNAFs and achiral NAFs (Figure S16e), respectively, which may be resulted from the large number of hot spots in chiral nanostructured Au fibres. The twisting of chiral molecules on the synthesis of Au nanofibres produced the chiral fibre structure and a multitude of crystalline defects that act as hot spots where Raman scattering can be substantially amplified. The sharp corners of the tetrahedral crystal units were also suggested playing a part in this phenomenon^[11].

The chemical adsorption and optical properties of CNAFs were analysed to investigate the chiral discrimination mechanism. X-ray photoelectron spectroscopy (XPS) of R-CNAFs provided no peaks, indicating absence of organic compounds in R-CNAFs (Figure S17). When R-CNAFs was loaded with S- and R-NAC, the XPS spectra showed peaks at approximately 400 eV, which is attributed to the N 1s of NAC. The peaks had almost identical areas, implying that equal amounts of antipodal NAC were adsorbed on the R-CNAF surface, which indicates no enantiomeric selectivity upon chemical adsorption in R-CNAF.

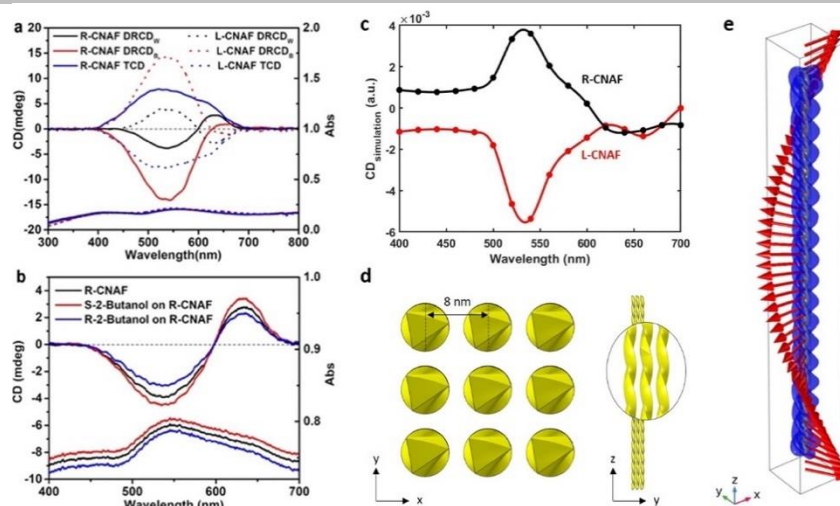


Figure 4. Selective enhancement of resonance between CNAFs and enantiomers. a) UV-Vis and CD spectra of antipodal CNAFs grown on quartz substrate measured with TCD and DRCD_W and DRCD_B, respectively. b) Diffuse-reflection UV-Vis with white background (DRUV-Vis_W) and DRCD_W spectra of R-CNAFs and loading with S- and R-2-Butanol. c) Simulated differential extinction cross-section for modeled L- and R-tetrahelices. d) Geometry of modeled tetrahelices to mimic experimental conditions with diameter of helices set as 5 nm and the center-center separation of 8 nm with a length of 400 nm. e) Spatial distribution of scattered electric field (blue isosurface at 6.6×10^8 V/m) around a modeled left-handed helix (yellow) in left-handed circularly polarized electric field (red arrows) of wavelength 460 nm.

The SERS selectivity of SERS-ChA effect of one enantiomers over the other counterparts can be evidenced by ultraviolet-visible (UV-Vis) and circular dichroism (CD) spectra. Figure 4a shows the UV-Vis and CD spectra of antipodal CNAFs grown on transparent quartz wafer. Experimental mirror-imaged CD spectra of R- and L-CNAF reflected the selective interaction between the CNAFs and circularly polarized light due to the dissymmetric centers existing in the plasmonic resonance state of CNAFs. The transmitted CD (TCD) spectra of antipodal CNAFs exhibited opposite signals at ~ 514 nm originated from both scattering-based OA (SOA) and plasmonic absorption-based OA (AOA) (Figure S18a). It is known that the diffuse-reflection CD with white (DRCD_W) and black (DRCD_B) background approximately show the solely AOA and both SOA and AOA, because almost all light would be reflected by white and absorbed by black background; and the signals of SOA with white and black background are opposite because transmitted and reflected light were detected by the TCD and DRCD system, respectively (Figure S18b and c). The DRCD_W spectrum of R-CNAF displayed a positive coupling centered at ~ 600 nm originated from the plasmonic absorption of CNAFs with right-handedness. Therefore, the TCD spectra can be considered as a combination of positive SOA and positive AOA (Figure S19a); and the DRCD_B spectra shows the combination of negative SOA and analogical positive AOA (Figure S19c); which confirmed again the right-handedness of R-CNAFs. The CD spectra showed such small circular polarization excess arising from antipodal CNAF that it can be negligible as circularly polarized incident light for SEROA. Thus, the circular polarization does not contribute to the SERS-ChA effect.

The selective enhancement of localized electromagnetic fields generated by different interaction between enantiomeric molecules and CNAFs were confirmed by DRUV-Vis_W and DRCD_W spectra of antipodal enantiomers loaded on R-CNAF. Compared to the raw R-CNAF, both plasmonic absorbance and corresponding DRCD_W signal of R-CNAF were enhanced with loading S-2-Butanol while weakened with R-2-Butanol (Figure 4b), which confirmed the selective enhancement of localized optical field due to the more intensive resonance between R-CNAF and S-2-Butanol over R-2-Butanol. The generated Raman

spectra of enantiomers were further enhanced by the local chiral electromagnetic field of R-CNAFs leading to SERS-ChA effect. Other three pairs of enantiomers shown in Figure 2 also displayed similar chiral-selective enhancement resonance between enantiomers and R-CNAFs (Figure S20).

By analogy to the electromagnetic theory of conventional SERS^[5] and previous studies on plasmonic enhancement of vibrational spectra^[12], the SERS-ChA on R-CNAF originate from the local chiral electromagnetic fields (Figure 4e) that interact asymmetrically with R- and S- enantiomers. The match between experimental and calculated CD spectra (Figure 4c-d, Figure S21-22) validate the electromagnetic field calculations and give additional evidence for strong asymmetry of the local fields in R-CNAF platform. These local fields in the assemblies of nanowires (Figure 2a) enhance Raman scattering for both enantiomers but for one of them is substantially stronger due to the match with chirality of the molecules.

To the best of our knowledge, the SERS-ChA effect is the first example of efficient chiral response of pure inorganic materials used for determining the absolute configuration and enantiomeric excess. The system displays a versatility covering almost all enantiomers regardless of their polarity, size, and chromophore content, which is promising for enantiomeric discrimination technologies and open new horizons for chiral responses in chemistry, physics and biology. The effect also provides daunting challenges and opportunities in various research areas, such as chiral theory, chiroptical spectroscopy, asymmetric catalysis, chiral bio-response, and manufacturing of optical, electrical, and mechanical device developments.

Acknowledgements

We thank Prof. Bin Ren, Mr. Yifan Bao and Miss Sisi Wu (Xiamen University), Prof. Yitao Long, Mr. Binbin Chen and Miss Jian Lv (East China University of Science and Technology). This work was supported by the National Natural Science Foundation of China (Grant No. 21931008, S.C.; 21975184, Y.D.; 21922304 and 21873072, L.H.; 21673273 and 21872163, X.L), GAČR (18-05770S; P.B) and MŠMT (LTC17012; P.B.).

Conflict of interest

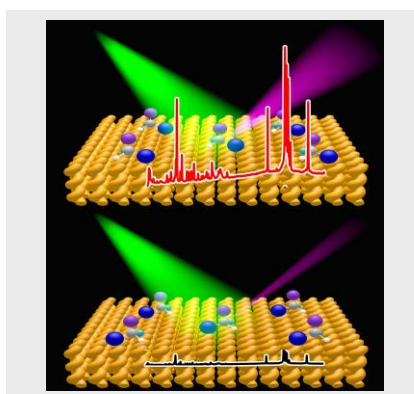
The authors declare no conflict of interest.

Keywords: surface-enhanced Raman scattering • chiral anisotropy • enantiomeric discrimination • chiral response • chiral nanostructured Au film

- [1] a) J. Shen, Y. Okamoto, *Chem. Rev.* **2016**, *116*, 1094-1138; b) T. D. James, K. Sandanayake, S. Shinkai, *Nature* **1995**, *374*, 345-347; c) D. Patterson, M. Schnell, J. M. Doyle, *Nature* **2013**, *497*, 475-478; d) K. Banerjee-Ghosh, O. Ben Dor, F. Tassinari, E. Capua, S. Yochelis, A. Capua, S. H. Yang, S. S. P. Parkin, S. Sarkar, L. Kronik, L. T. Baczewski, R. Naaman, Y. Paltiel, *Science* **2018**, *360*, 1331-1334; e) S. Dutta, A. J. Gellman, *Chem. Soc. Rev.* **2017**, *46*, 7787-7839; f) P. Lesot, C. Aroulanda, H. Zimmermann, Z. Luz, *Chem. Soc. Rev.* **2015**, *44*, 2330-2375.
- [2] a) L. D. Barron, *Molecular Light Scattering and Optical Activity*, Cambridge University Press, **1982**; b) N. Berova, L. Di Bari, G. Pescitelli, *Chem. Soc. Rev.* **2007**, *36*, 914-931; c) L. Yang, C. S. Kwan, L. L. Zhang, X. H. Li, Y. Han, K. C. F. Leung, Y. G. Yang, Z. F. Huang, *Adv. Funct. Mater.* **2019**, *29*, 8; d) B. T. Thole, P. Carra, F. Sette, G. Vanderlaan, *Phys. Rev. Lett.* **1992**, *68*, 1943-1946; e) L. A. Nafie, *Vibrational Optical Activity: Principles and Applications*, Blackwell Science Publ, Oxford, **2011**; f) N. Berova, K. Nakanishi, R. W. Woody, *Circular dichroism: principles and applications*, Wiley-VCH, **2000**; g) N. Bouldi, N. J. Vollmers, C. G. Delpy-Laplanche, Y. Joly, A. Juhin, P. Saintavit, C. Brouder, M. Calandra, L. Paulatto, F. Mauri, U. Gerstmann, *Phys. Rev. B* **2017**, *96*, 12.
- [3] a) D. Sofikitis, L. Bougas, G. E. Katsoprinakis, A. K. Spiliotis, B. Loppinet, T. P. Rakitzis, *Nature* **2014**, *514*, 76-79; b) S. Beaulieu, A. Comby, D. Descamps, B. Fabre, G. A. Garcia, R. Geneaux, A. G. Harvey, F. Legare, Z. Masin, L. Nahon, A. F. Ordonez, S. Petit, B. Pons, Y. Mairesse, O. Smirnova, V. Blanchet, *Nat. Phys.* **2018**, *14*, 484-489.
- [4] a) K. Kneipp, Y. Wang, H. Kneipp, L. T. Perelman, I. Itzkan, R. Dasari, M. S. Feld, *Phys. Rev. Lett.* **1997**, *78*, 1667-1670; b) S. Y. Ding, J. Yi, J. F. Li, B. Ren, D. Y. Wu, R. Panneerselvam, Z. Q. Tian, *Nat. Rev. Mater.* **2016**, *1*, 16; c) M. Fleischmann, P. J. Hendra, A. J. McQuillan, *Chem. Phys. Lett.* **1974**, *26*, 163-166.
- [5] a) M. Moskovits, *Rev. Mod. Phys.* **1985**, *57*, 783-826; b) E. C. Le Ru, P. G. Etchegoin, **2009**, 629-653.
- [6] S. Abdali, E. W. Blanch, *Chem. Soc. Rev.* **2008**, *37*, 980-992.
- [7] a) L. D. Barron, A. D. Buckingham, *Annu. Rev. Phys. Chem.* **1975**, *26*, 381-396; b) L. D. Barron, **2013**.
- [8] J. He, Y. Wang, Y. Feng, X. Qi, Z. Zeng, Q. Liu, W. S. Teo, C. L. Gan, H. Zhang, H. Chen, *Acs Nano* **2013**, *7*, 2733-2740.
- [9] a) Y. H. Zhu, J. T. He, C. Shang, X. H. Miao, J. F. Huang, Z. P. Liu, H. Y. Chen, Y. Han, *J. Am. Chem. Soc.* **2014**, *136*, 12746-12752; b) A. H. Boerdijk, *Philips Res. Rep.* **1952**, *7*, 303-313; c) J. Yan, W. C. Fang, J. Y. Kim, J. Lu, P. Kumar, Z. Z. Mu, X. C. Wu, X. M. Mao, N. A. Kotov, *Chem. Mater.* **2020**, *32*, 476-488.
- [10] P. Oleynikov, *Cryst. Res. Technol.* **2011**, *46*, 569-579.
- [11] a) J. Zhou, J. An, B. Tang, S. P. Xu, Y. X. Cao, B. Zhao, W. Q. Xu, J. J. Chang, J. R. Lombardi, *Langmuir* **2008**, *24*, 10407-10413; b) C. G. Khoury, T. Vo-Dinh, *J. Phys. Chem. C* **2008**, *112*, 18849-18859.
- [12] M. Yang, R. Alvarez-Puebla, H. S. Kim, P. Aldeanueva-Potel, L. M. Liz-Marzan, N. A. Kotov, *Nano Lett.* **2010**, *10*, 4013-4019.

COMMUNICATION

We report a surface-enhanced Raman scattering chiral anisotropy effect that combines chiral discrimination and surface Raman scattering enhancement on chiral nanostructured Au films applied in the normal Raman scattering system, for identifying absolute configuration and composition of enantiomers, which overcome disadvantages of polarimeter systems and chromatography.



Zexi Liu,[†] Jing Ai,[†] Prashant Kumar,[†] Enming You,[†] Xiong Zhou,[†] Xi Liu,[†] Zhongqun Tian, Petr Bouř, Yingying Duan,^{*} Nicholas A. Kotov,^{*} Songyuan Ding,^{*} Lu Han^{*} and Shunai Che^{*}

Page No. – Page No.

Enantiomeric Discrimination by Surface-Enhanced Raman Scattering-Chiral Anisotropy of Chiral Nanostructured Gold Films